

Formation of Nanowindow between Graphene Oxide and Carbon Nanohorn Assisted by Metal Ions

Zhao Li, Moeto Toyota, and Takahiro Ohkubo*



Cite This: <https://doi.org/10.1021/acs.langmuir.4c04479>



Read Online

ACCESS |



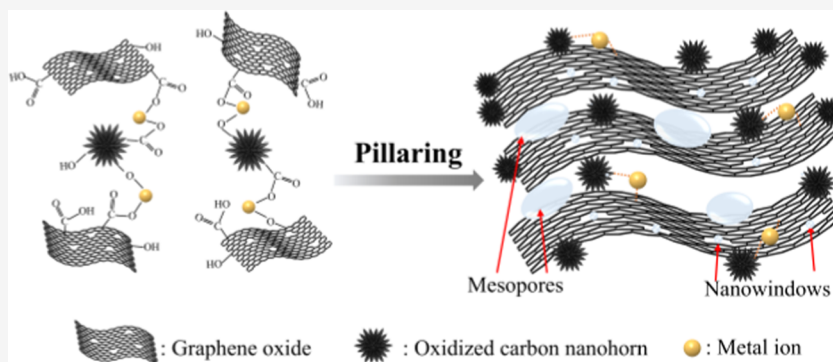
Metrics & More



Article Recommendations



Supporting Information



ABSTRACT: This study presents a novel nanostructured material formed by inserting oxidized carbon nanohorns (CNHox) between layered graphene oxide (GO) nanosheets using metal ions (M) from nitrate as intermediates. The resulting GO–CNHox–M structure effectively mitigated interlayer aggregation of the GO nanosheets. This insertion strategy promoted the formation of nanowindows on the surface of the GO sheets and larger mesopores between the GO nanosheets, improving material porosity. Characterization revealed successful CNHox insertion, which increased interlayer spacing and reduced GO stacking. The GO–CNHox–Ca exhibited a significantly higher specific surface area (SSA) and pore volume than pure GO, with values of $374 \text{ m}^2 \text{ g}^{-1}$ and 0.36 mL g^{-1} , respectively. The GO–CNHox–K composite also exhibited a well-developed pore structure with an SSA of $271 \text{ m}^2 \text{ g}^{-1}$ and pore volume of 0.26 mL g^{-1} . These findings demonstrate that Ca^{2+} or K^+ ions effectively link GO and CNHox, validating the success of this insertion approach in reducing GO aggregation. Metal ions played a crucial role in the insertion process by facilitating electrostatic interactions and coordination bonds between GO and CNHox. This study provides new insights into reducing GO agglomeration and expanding the application of GO-based materials.

INTRODUCTION

Carbon materials have significant potential in modern science, particularly in energy storage, catalysis, adsorption, sensing, and pollution mitigation applications.^{1–3} Among these materials, graphene oxide (GO) has garnered substantial attention due to its abundant oxygen functional groups (OFGs), such as carboxyl (COOH), hydroxyl (OH), carbonyl (C=O), and epoxy (C–O–C) groups.^{4,5} These functional groups are dispersed across the carbon skeleton, with carboxyl and hydroxyl groups located primarily at the edges of GO, and carbonyl and epoxy groups on the basal plane.^{6–9} These diverse OFGs impart excellent chemical properties to GO, broadening its applications, including heavy metal ion removal,^{10,11} gaseous molecule adsorption,^{12,13} and drug delivery.¹⁴

However, the interlayer structure of GO is typically densely stacked, obstructing the exposure of surface adsorption sites and limiting the functionality of its OFGs on the GO surface.^{15,16} To address this issue, numerous researchers have explored the insertion of additional materials into the interlayer

spaces of GO sheets. For instance, Zhang et al. enhanced water permeability and stability by inserting multiwalled carbon nanotubes into GO, achieving a permeation flux of $34.4 \text{ L m}^{-2} \text{ h}^{-1}$ and a rejection rate of over 99.7% for methylene blue.¹⁷ Similarly, Giordani et al. synthesized nanocomposite materials with a high specific surface area (SSA) of $660 \text{ m}^2 \text{ g}^{-1}$ by introducing tetrakis (4-aminophenyl) methane (TKAm) into GO nanosheets, achieving a maximum hydrogen adsorption of 1.66 wt % at 77 K.¹⁸ Nguyen et al. used chitosan molecules as pillaring agents between GO sheets to form GO cross-linked chitosan composites, significantly improving the SSA ($450 \text{ m}^2 \text{ g}^{-1}$) and enhancing the adsorption of cationic dye (methylene

Received: November 7, 2024

Revised: December 26, 2024

Accepted: January 9, 2025

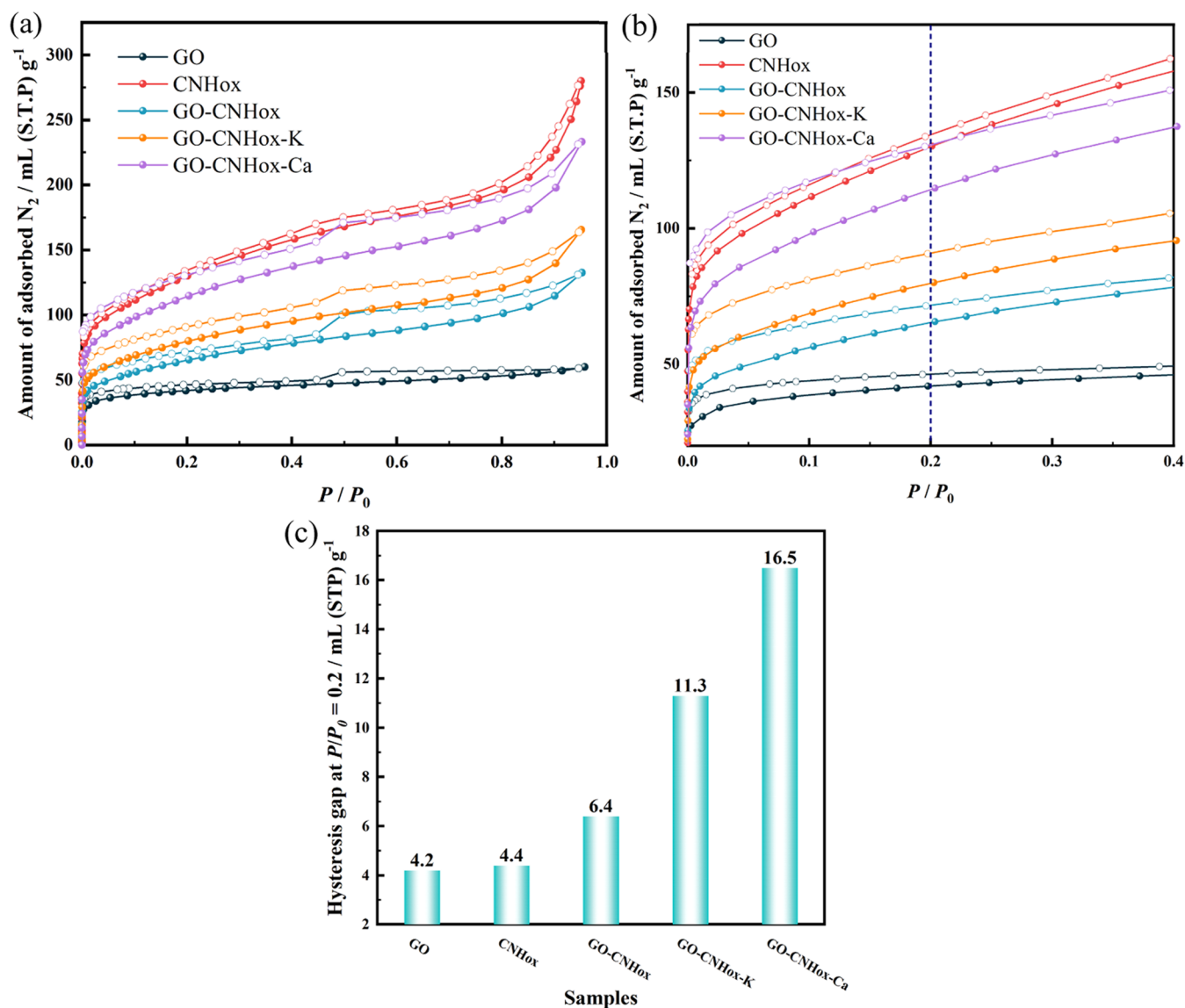


Figure 1. N₂ adsorption–desorption isotherms for (a) $P/P_0 = 0–1.0$ and (b) $P/P_0 = 0–0.4$ of GO, CNHox, GO–CNHox, GO–CNHox-K, and GO–CNHox-Ca at 77 K. Solid and hollow dotted lines represent the adsorption and desorption branches, respectively. (c) Hysteresis gap of each sample at $P/P_0 = 0.2$.

blue) in aqueous solution.¹⁹ Despite these advances, the utilization of organic spacers and complex synthesis processes has limited the widespread application of these composites.

Carbon nanohorns (CNH) have attracted considerable attention due to their unique assembly of single-walled tube-like units with an average diameter of approximately 80 nm.^{20–23} CNH primarily comprises sp^2 carbon atoms, with a small portion of sp^3 carbon atoms, making them highly hydrophobic.^{24,25} Although previous studies have successfully used carbon nanotubes as supporting pillars for GO nanosheets,^{17,26,27} the potential of oxidized carbon nanohorns (CNHox) with OFGs as pillaring agents remains unexplored. The surface characteristics of CNHox endow it with the ability to form a unique composite structure through both van der Waals forces and electrostatic interactions with GO layers, effectively facilitating the insertion process. Especially, CNHox exhibits high dispersibility in water, making it easier to insert into the interlayer structure of GO. Therefore, CNHox could potentially reduce the stacking of GO sheets, resulting in novel

composite structures. To date, no studies have explored the incorporation of CNHox into GO nanosheets. Hence, this study aims to introduce CNHox into GO to form new composite materials with improved properties and potential applications.

The formation of tight bonds in composites is essential. Metal ions can react with OFGs on the surface of GO and CNHox via chemical bonds, facilitating effective connections.²⁸ In this study, we fabricated a GO–CNHox-M nanocomposite by pillaring CNHox into GO nanosheets using metal cations (M: K or Ca) from nitrates. The composite exhibited a higher SSA and a more advanced pore structure than pure GO. This is attributed to the M-ion-modified CNHox, which effectively grafts onto the GO nanosheets, promoting the formation of a nanowindow structure on the GO surface and creating more mesoporous structures. This enhanced pore structure is expected to improve the adsorption capacity of the material in air.

MATERIALS AND METHOD

Chemicals and Materials. Graphite powder (99.9995%) was obtained from Alfa Aesar. Potassium permanganate (KMnO_4 , 99.3%), concentrated sulfuric acid (H_2SO_4 , 97%), potassium nitrate (KNO_3 , 99.9%), calcium nitrate tetrahydrate ($\text{Ca}(\text{NO}_3)_2 \cdot 4\text{H}_2\text{O}$, 99.9%), and hydrogen peroxide (H_2O_2 , 30%) were purchased from Fujifilm Wako Pure Chemical Corp., Japan. Hydrochloric acid (HCl , 35%) was supplied by Nacalai Tesque, Inc., Japan. Carbon nanohorns were provided by Nippon Electric Company, Japan.

Synthesis of GO Sample. GO was synthesized using the modified Hummers' method.^{29,30} Initially, 1.0 g of 200 mesh graphite powder was added to 25 mL of concentrated H_2SO_4 and stirred in an ice bath. Then, 3.0 g of KMnO_4 was slowly introduced, ensuring the temperature remained below 10 °C. The reaction mixture was transferred to a 35 °C water bath and stirred for 2 h. Afterward, 100 mL of deionized (DI) water was added dropwise, and the solution was heated to 90 °C for 15 min. The mixture was allowed to cool to room temperature. To reduce Mn^{7+} , 5 mL of 30% H_2O_2 was gradually added to the reaction mixture. The product was washed three times with a 5% HCl aqueous solution to remove residual Mn ions, and the precipitate was centrifuged with DI water until the pH reached 7. The obtained GO was dispersed in an aqueous solution and the dispersion was placed in a dialysis bag for a 15-day dialysis period with daily water changes. Following dialysis, the dispersed mixture was filtered through a 5 μm membrane to form a filter cake, which was then dried at 80 °C for 8 h and finely ground into powder (1.74 g). The weight ratio of GO to graphite powder was 1.74, corresponding to a yield of 174%.

Synthesis of CNHox-M Samples. CNH was oxidized by adding 250 mg of CNH to 250 mL of an aqueous solution of 10% HNO_3 , and the mixture was treated at 90 °C for 24 h, resulting in oxidized carbon nanohorn (CNHox). Subsequently, 50 mg of CNHox was mixed with 100 mL of DI water and sonicated for 60 min to obtain a uniformly dispersed CNHox solution. For the preparation of CNHox-M (M: K or Ca), 0.5 mmol of KNO_3 or $\text{Ca}(\text{NO}_3)_2 \cdot 4\text{H}_2\text{O}$ was added to the CNHox dispersed solution. The resulting mixture was stirred for 24 h to ensure metal ions were adsorbed onto the CNHox surface. The mixture was then filtered through a membrane and dried at 80 °C for 8 h. These samples were labeled as CNHox-K or CNHox-Ca.

Synthesis of GO–CNHox-M Samples. The GO dispersion was obtained by adding 60 mg of GO to 300 mL of DI water and sonication for 90 min until a uniform GO monolayer was formed. Subsequently, 30 mg of CNHox-K or CNHox-Ca was added to the dispersed GO solution. After sonication for 2 h, the solution was stirred for 2 d. The dispersed mixture was filtered through a 0.2 μm membrane to form GO–CNHox-K or GO–CNHox-Ca film. The films were dried at 80 °C for 8 h and then ground into powder. These samples were designated as GO–CNHox-K or GO–CNHox-Ca.

Characterization. Nitrogen adsorption–desorption isotherms at 77 K were obtained using a BELSORP-max-SP instrument (MicrotracBEL Corp., Japan). The pore structure was analyzed by the α_s -plot method, which included SSA and pore volume calculations.^{31,32} The CO_2 adsorption capacity was measured at 30 °C using the BELSORP-max-SP instrument (MicrotracBEL Corp., Japan). X-ray diffraction (XRD) data were obtained using a MiniFlex II instrument (Rigaku Corp., Japan) with $\text{Cu K}\alpha$ radiation (0.154 nm) over a 5°–35° range. Fourier-transform infrared (FTIR) spectra were recorded using a Digilab FTS4000MXK spectrophotometer (Randolph) via the KBr method at room temperature, within the 800–2000 cm^{-1} range. Thermal gravimetric analysis (TGA) was conducted using a Thermal Plus EVO2 instrument (Rigaku Corp., Japan) in an air atmosphere. X-ray photoelectron spectroscopy (XPS) was performed using a JPS-9030 instrument (JEOL Ltd., Japan) with an $\text{Mg K}\alpha$ X-ray source (1253.6 eV). Scanning electron microscopy (SEM) images were acquired using an SU 9000 field-emission scanning electron microscope (Hitachi Corp., Japan).

RESULTS AND DISCUSSION

Pore and Composite Structure of GO–CNHox-M.

Figure 1a shows the N_2 adsorption–desorption isotherms of the samples. According to the latest IUPAC classification, the adsorption isotherms of all samples correspond to type IV, indicating the presence of micropores, mesopores, and a small number of macropores.³³ Table S1 provides the detailed parameters obtained from N_2 adsorption–desorption curves for GO, CNHox, GO–CNHox, GO–CNHox-K, and GO–CNHox-Ca. As depicted in Figure 1a, GO exhibits a total surface area and pore volume of 155 $\text{m}^2 \text{g}^{-1}$ and 0.10 mL g^{-1} , respectively, while CNHox shows significantly higher values of 431 $\text{m}^2 \text{g}^{-1}$ and 0.44 mL g^{-1} . The lower values for GO are primarily due to the stacking of GO sheets, which limits the exposure of its pore structure. The GO–CNHox sample has an SSA of 214 $\text{m}^2 \text{g}^{-1}$ and a pore volume of 0.21 mL g^{-1} , which are higher than those of GO but lower than those of CNHox. In addition, the total SSA of GO–CNHox-K is 271 $\text{m}^2 \text{g}^{-1}$, and the total pore volume is 0.26 mL g^{-1} . The SSA and pore volume of GO–CNHox-Ca are 374 $\text{m}^2 \text{g}^{-1}$ and 0.36 mL g^{-1} , respectively. The total SSA and pore volumes of these two materials were higher than the corresponding values of the GO–CNHox sample, suggesting the successful insertion of CNHox-M into the GO structure. This enhancement is attributed to the metal ions attracting the negatively charged OFGs on CNHox and GO via electrostatic interactions. Additionally, cations form coordination bonds between GO and CNHox, facilitating the adhesion of CNHox to the GO surface and alleviating the stacking of GO nanosheets. The insertion of CNHox-M into the GO structure results in the formation of a new composite with a more developed porous structure, significantly increasing the SSA and pore volume. This enhancement is particularly evident in GO–CNHox-Ca, which exhibits stronger electrostatic interactions and coordination bonds, leading to increased CNHox adhesion to the GO surface and exposing more adsorption sites on the nanosheets. Notably, the rate of increase in mesopore SSA and pore volume values in the composites is greater than that of the micropores. For example, the mesopore SSA and pore volume values of GO–CNHox-Ca are 5.6 times and 5.8 times greater, respectively, than those of GO, whereas the micropore SSA and pore volume values are 1.8 times and 2.2 times higher, respectively. This is due to the formation of new mesoporous structures between the spaces of the interlayer GO nanosheets. Therefore, the porosity of the composite can be effectively increased by inserting CNHox into GO with the assistance of metal ions.

Figure 1b shows the N_2 adsorption–desorption isotherms for $P/P_0 < 0.4$. According to the shapes of the isotherms, all the samples exhibit apparent adsorption hysteresis, even in the low-pressure region, which is attributed to the possible presence of nanowindows on the material. Nanowindows are nanoscale holes formed on a graphene monolayer, with sizes comparable to the diameters of adsorbed gases such as N_2 and Ar.³⁴ The process of embedding and releasing adsorbed molecules into the pore through such nanowindows requires overcoming potential barriers, resulting in low-pressure hysteresis during the adsorption and desorption processes.³⁵ The low-pressure hysteresis gap between the desorption and adsorption branches serves as a reliable indicator for evaluating the permeation limit of nanowindows. As shown in Figure 1b,c, the low-pressure hysteresis gap of GO and CNHox is 4.22 and

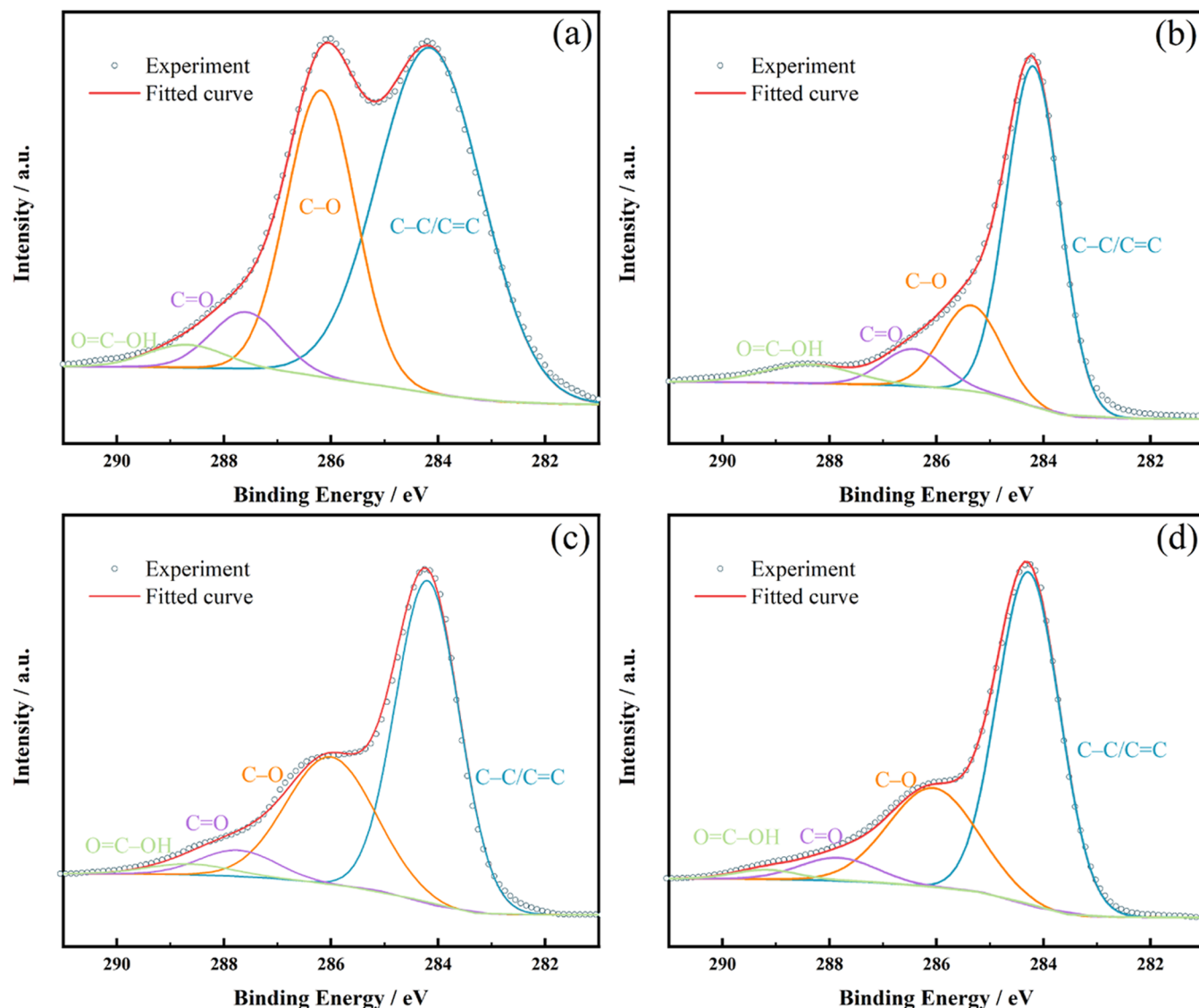


Figure 2. XPS C 1s high-resolution spectra of (a) GO, (b) CNHox, (c) GO-CNHox, and (d) GO-CNHox-Ca.

4.43 mL g⁻¹, respectively, showing similar hysteresis characteristics. These nanowindows originate from the oxidation process of GO and CNHox, respectively. Specifically, the nanowindows in GO are mainly formed by the synergistic oxidation of carbon atoms by concentrated sulfuric acid and potassium permanganate, while the nanowindows in CNHox are produced by the oxidation of carbon atoms dispersed in aqueous nitric acid. The composite material formed by introducing CNHox into the space between GO sheets showed a more pronounced low-pressure adsorption hysteresis. As shown in Figure 1b,c, the low-pressure adsorption hysteresis gap for GO-CNHox and GO-CNHox-K is 6.4 and 11.3 mL g⁻¹, respectively, which are significantly higher than those of pure GO and CNHox samples. The hysteresis effect is more pronounced in the GO-CNHox-M samples due to the presence of metal ions, with GO-CNHox-Ca exhibiting the highest hysteresis gap of 16.5 mL g⁻¹, indicating the presence of the largest number of nanowindows. This phenomenon occurs because the insertion of CNHox-Ca between the spaces of the GO nanosheets alters their stacking arrangement and creates new nanowindows between GO and CNHox-M.

The morphological structures of GO, CNHox, and GO-CNHox-Ca were characterized by SEM. As shown in Figure S1, GO exhibits an apparent lamellar structure, consistent with previous reports.²² CNHox displays an assembled configuration of individual oxidized carbon nanohorns. Figure S1c-e show the SEM images of GO-CNHox, GO-CNHox-K, and GO-CNHox-Ca. From these figures, it can be seen that all samples were effectively adsorbed onto the surface of the GO nanosheets. Notably, a comparison of the SEM images of different samples reveals that more CNHox adhered to the surface of GO-CNHox-M than to GO-CNHox, indicating that the presence of cations effectively promotes the insertion of CNHox into the interspaces between GO nanosheets. Additionally, more CNHox adhered to the surface of GO-CNHox-Ca than GO-CNHox-K, suggesting that Ca²⁺ more effectively promotes the adhesion of CNHox to GO nanosheets than K⁺. This is due to Ca²⁺ enhancing CNHox adhesion through stronger electrostatic attraction and coordination bonds. Therefore, SEM results demonstrate that metal ions strengthen the connection between CNHox and GO.

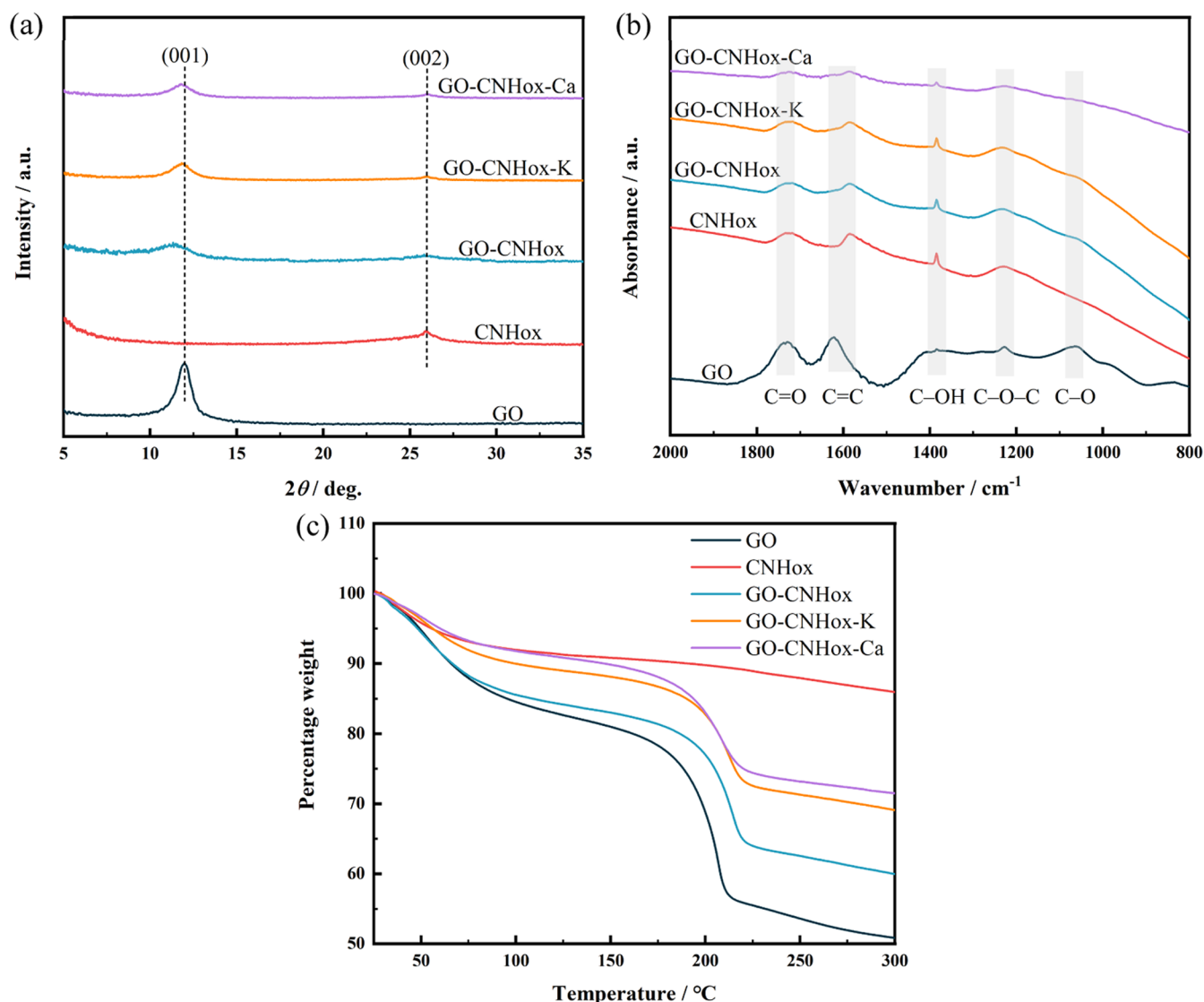


Figure 3. (a) XRD patterns, (b) FTIR spectra, and (c) TGA profiles of GO, CNHox, GO-CNHox, GO-CNHox-K, and GO-CNHox-Ca.

Surface Chemical Composition. Figure S2 illustrates the wide-range XPS spectra of GO, CNHox, GO-CNHox, and GO-CNHox-Ca, with the C 1s peak at 284 eV, O 1s peak at 532 eV, and Ca 2p peak at 349 eV detected at specific binding energies.^{36–38} These results are crucial for determining the elemental compositions and C/O ratios of the samples. As shown in Table S2, GO and CNHox are primarily composed of carbon and oxygen, confirming the successful oxidation of graphite powder and carbon nanohorns, respectively. GO contains 65.7% carbon and 34.3% oxygen, whereas CNHox contains 86.4% carbon and 13.6% oxygen, with GO exhibiting a lower carbon content and higher oxygen content than CNHox. GO-CNHox is composed of 68.2% carbon and 31.8% oxygen, with values intermediate between those of GO and CNHox, indicating the composite nature of GO-CNHox, which combines the components of GO and CNHox. Similarly, GO-CNHox-Ca contains both GO and CNHox components with the incorporation of Ca. The higher carbon content and lower oxygen content in GO-CNHox-Ca compared to GO-CNHox further indicate a higher proportion of CNHox in the former. These data further confirm that Ca^{2+}

promotes the attachment of more CNHox on the surface of GO nanosheets compared to samples without Ca^{2+} .

Figure 2 illustrates four deconvoluted bands in the C 1s spectrum, each corresponding to distinct carbon bonding states: sp^2 and sp^3 carbon (C=C and C-C, 284.2 eV), epoxy (C-O, 286.2 eV), carbonyl (C=O, 287.7 eV), and carboxyl (O=C-OH, 288.9 eV). The data for all four samples are summarized in Table S3. Figure 2a,b show that the content of OFGs in GO is higher than in CNHox, which corresponds to the results shown in Figure S2. Additionally, GO exhibits the highest C-O content, while CNHox displays the lowest. Since GO-CNHox and GO-CNHox-Ca contain both GO and CNHox, their C-O contents are between the ratios of the two components. Figure 2c,d reveal that GO-CNHox-Ca has a lower C-O content than GO-CNHox. This can be attributed to two factors: first, the content of CNHox in GO-CNHox-Ca is higher; second, Ca^{2+} acts as a Lewis acid, inducing the ring-opening reaction of epoxy groups to form C-O-Ca groups.^{28,39} The slight shift of the C-O band from 286.0 to 286.1 eV indicates a coordination interaction between the Ca^{2+} ion and the C-O group. Moreover, the C 1s binding energy corresponding to the carboxyl group shifts from 288.5 to 289.1

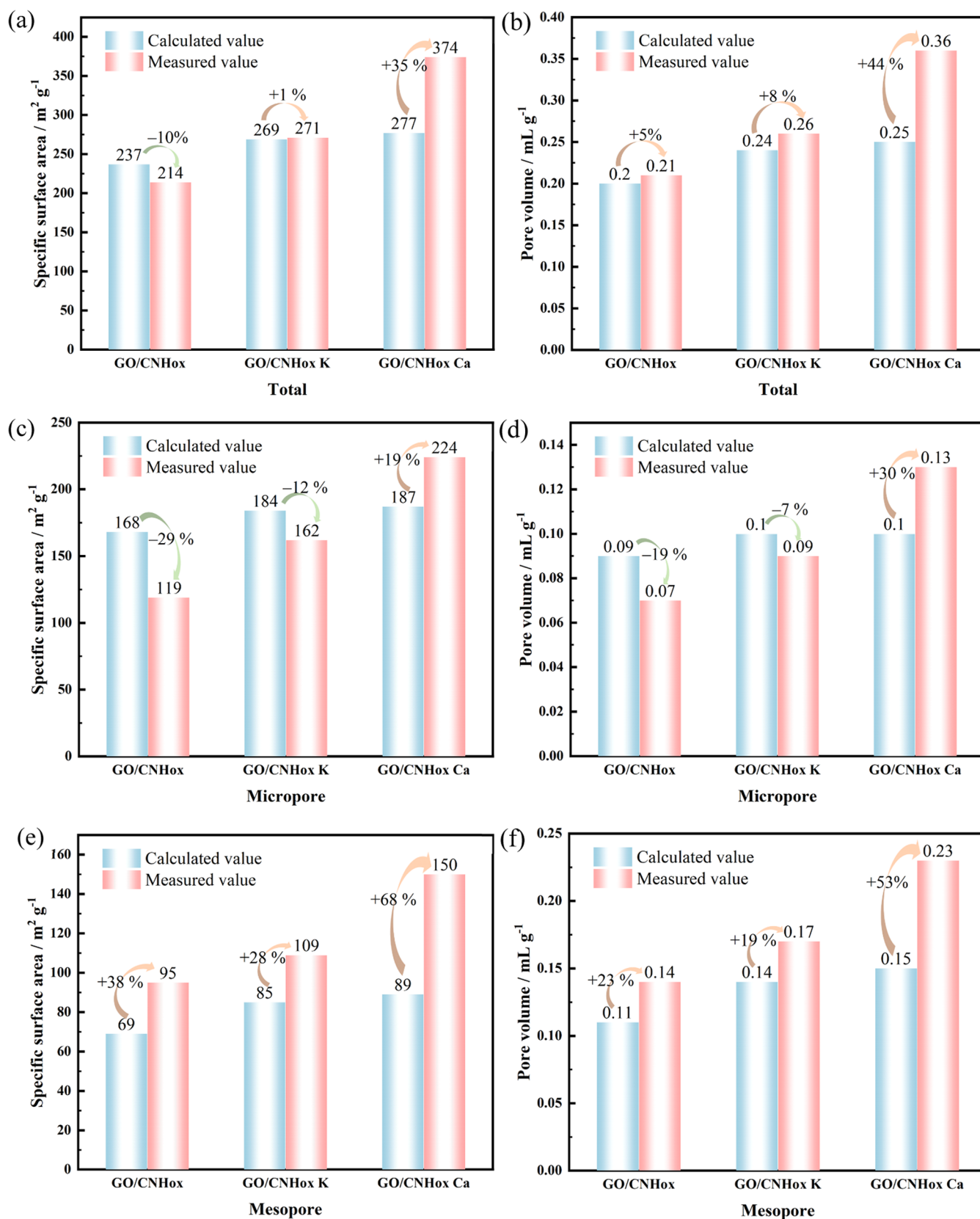


Figure 4. Comparison of pore-structure parameters between calculated and actual measured data of GO–CNHox, GO–CNHox-K, and GO–CNHox-Ca. (a), (c), and (e) denote the specific surface areas of total, micropore, and mesopore, respectively. (b), (d), and (f) represent the pore volume of total, micropore, and mesopore, respectively. (The ideal value is calculated by estimating the weight ratio of the composite from XPS data. The growth rate of actual test data compared to theoretical data.)

eV, indicating coordination between the metal ions and carboxyl groups.³⁹ These results indicate that Ca^{2+} can directly coordinate with carboxyl groups, promoting the formation of the GO–CNHox–Ca structure and strengthening the connection between CNHox and GO.

Microcrystalline and Surface Structure. The XRD patterns of GO, CNHox, GO–CNHox, GO–CNHox–K, and GO–CNHox–Ca are shown in Figure 3a and Table S4. The (001) diffraction profile of GO was located at 11.97° , corresponding to an interplanar spacing of 0.739 nm.^{7,8} CNHox exhibits a graphite (002) peak at 25.96° , indicating the presence of graphite impurities. The d -spacing of the samples was determined using Bragg's equation. The calculated results are shown in Table S4, indicating that the d -spacings of GO–CNHox, GO–CNHox–K, and GO–CNHox–Ca were 0.782, 0.747, and 0.748 nm, respectively. It is evident that GO–CNHox, GO–CNHox–K, and GO–CNHox–Ca exhibit larger d -spacings than the 0.739 nm spacing of GO. Although the difference in d -spacings before and after the addition of CNHox is very small, the broadening in the profiles is another indication of the effective insertion. These results suggest that CNHox, CNHox–K, and CNHox–Ca were effectively embedded within the GO structure.

The FTIR spectra in Figure 3b display several absorption bands in the GO sample at 1720, 1625, 1384, 1240, and 1090 cm^{-1} , corresponding to the carboxyl/carbonyl $\text{C}=\text{O}$, aromatic $\text{C}=\text{C}$, carboxyl $\text{C}-\text{O}$, epoxy/ether $\text{C}-\text{O}$, and alkoxy/alkoxide $\text{C}-\text{O}$ bonds, respectively. CNHox exhibits absorption bands at 1720, 1600, 1380, and 1240 cm^{-1} . The most significant difference between the CNHox and GO samples is the shift in the $\text{C}=\text{C}$ absorption band from 1625 to 1600 cm^{-1} . As shown in Figure 3b, the introduction of CNHox–Ca into the GO structure reduces the intensity of the $\text{C}-\text{O}-\text{C}$ and $\text{C}-\text{OH}$ bands, which is attributed to the Ca^{2+} inducing the ring opening of $\text{C}-\text{O}-\text{C}$ groups to form $\text{C}-\text{O}-\text{Ca}$ groups. Ca^{2+} also tends to attack the $\text{O}-\text{H}$ of the hydroxyl groups, forming new $\text{C}-\text{O}-\text{Ca}$ bonds, resulting in a decrease in hydroxyl content.²⁸ In GO–CNHox–M, metal ions can interact directly with OFGs on the surfaces of GO and CNHox, forming bonds such as $\text{C}-\text{O}-\text{M}$ and $\text{COO}-\text{M}$.^{40,41} Therefore, metal ions play a crucial role in establishing a strong connection between GO and CNHox.

Figure 3c and Table S5 show the TGA results. The weight loss due to adsorbed water for GO was 15.5%, which exceeded those of the other composites, indicating that GO had the highest adsorbed water content. This was attributed to the higher OFGs content in GO than in the other samples. More OFGs facilitated the retention of water molecules in the GO structure. In contrast, CNHox displayed the least amount of adsorbed water owing to its limited OFG content. Notably, the mass loss of OFGs for GO was 29.0%, which was significantly higher than that for CNHox (3.0%). In addition, GO–CNHox (21.3%) exhibited a greater loss of OFGs than GO–CNHox–K (18.3%) or GO–CNHox–Ca (17.6%). This phenomenon suggests that GO–CNHox contains less CNHox as a spacer than GO–CNHox–K and GO–CNHox–Ca. This is due to the influence of the metal ions, which strengthen the connection between GO and CNHox through electrostatic attraction and coordination bonds. By comparing the weight losses of the GO–CNHox–K and GO–CNHox–Ca OFGs, Ca^{2+} has stronger electrostatic and coordination effects to connect CNHox and GO more effectively.

Insertion Effect of Composites. The ideal and actual pore parameters of GO–CNHox, GO–CNHox–K, and GO–CNHox–Ca are shown in Figure 4 and Table S7, with the procedure for calculating these ideal values described in the Supporting Information. As shown in Figure 4, significant differences were observed between the total measured SSA and pore volumes of GO–CNHox, GO–CNHox–K, and GO–CNHox–Ca, compared to their calculated values. Specifically, the measured total SSA and pore volumes of GO–CNHox and GO–CNHox–K were relatively close to the calculated values. According to Figure 4, the growth rates of the measured values compared to the calculated values for GO–CNHox were -10 and 5% , respectively, while for GO–CNHox–K, the growth rates were 1 and 8% , respectively. In contrast, the measured total SSA for GO–CNHox–Ca was $374 \text{ m}^2 \text{ g}^{-1}$, significantly higher than its calculated value of $277 \text{ m}^2 \text{ g}^{-1}$. Similarly, the measured total pore volume (0.36 mL g^{-1}) exceeded the calculated value (0.25 mL g^{-1}). The growth rates of the measured values compared with the calculated values for GO–CNHox–Ca were 35 and 44% , respectively. These data indicate that the insertion of CNHox between GO nanosheets increased the SSA and pore volume of the composite materials. Notably, the SSA and pore volume of the composites were not simply additive from the individual components, CNHox and GO. The insertion of CNHox between GO nanosheets effectively reduced the severe stacking of GO, thereby exposing more adsorption sites on the GO surface. Therefore, this insertion effect significantly enhanced the overall SSA and pore volume of the composite materials, with a more pronounced effect in the mesoporous structure than in the microporous structure. As shown in Figure 4, the mesoporous SSA and pore volume of GO–CNHox increased by 38 and 23% , respectively, whereas those of GO–CNHox–K increased by 28 and 19% , respectively. However, the microporous SSA and pore volumes of both composites showed a slight decrease. In contrast, the mesoporous SSA and pore volume of GO–CNHox–Ca increased by 68 and 53% , respectively, whereas the microporous SSA and pore volume increased by 19 and 30% , respectively. This limited increase in micropores can be attributed to the smaller fraction of CNHox in contact with the GO nanosheets. Embedding CNHox within GO effectively supported the GO nanosheets, generating numerous mesoporous structures between them. A comparative analysis of the adsorption data revealed that the pore structures of GO–CNHox–Ca samples were more developed than those of GO–CNHox and GO–CNHox–K samples. These data are consistent with experimental measurements, indicating that Ca ions effectively bridge GO and CNHox, enhancing the insertion effect between the two materials.

Assessment of CO_2 Adsorption Capacity under Low-Pressure Conditions. Figure 5 shows a comparative analysis of the CO_2 adsorption capacities of GO, CNHox, and GO–CNHox–Ca under low-pressure conditions. In the present atmospheric composition, the CO_2 concentration exceeds 400 ppm, corresponding to a partial pressure of approximately 0.3 Torr.⁴² Thus, evaluating CO_2 adsorption capacity under these conditions provides essential insights into the CO_2 adsorption behavior as a direct-air capture material. The adsorption capacity of the sample is linearly increased to the test pressure up to 0.32 Torr, following the Henry's adsorption isotherm model.⁴³ In this range, the number of adsorption sites was large relative to that of adsorbent gas molecules, allowing all adsorption sites to be considered independent. At an absolute

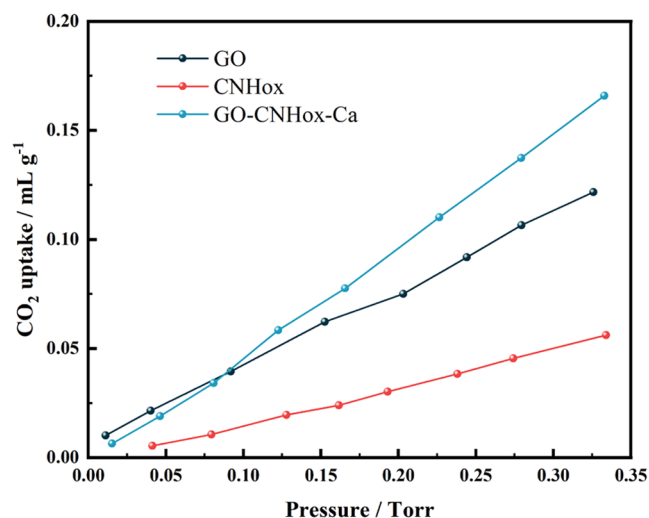


Figure 5. CO₂ adsorption under low-pressure conditions of GO, CNHox, and GO–CNHox–Ca at 303 K.

pressure of 0.32 Torr, the adsorbed CO₂ amounts on GO, CNHox, and GO–CNHox–Ca were 0.121, 0.056, and 0.166 mL g⁻¹, respectively. A comparative analysis revealed that GO–CNHox–Ca possessed a superior adsorption capacity compared to GO and CNHox. Several factors contributed to this observation. First, GO–CNHox–Ca possesses a more effective pore structure, which is more conducive to the adsorption of CO₂ molecules than GO and CNHox. Numerous nanowindows on the GO and CNHox surfaces, as well as micropores formed at the interfacial region between the two materials, enhanced the adsorption efficiency. These additional pore structures, slightly larger than the diameter of the CO₂ molecules, facilitated the effective capture of CO₂ through weak van der Waals forces.⁴⁴ Second, in the GO–CNHox–Ca sample, the insertion of CNHox into GO reduces the tight stacking of GO sheets. Compared to pure GO, this allows the exposure of more accessible functional groups (e.g., hydroxyl and carboxyl groups), which can capture CO₂ through electrostatic bonding.⁴⁵ Finally, the incorporation of Ca into the GO–CNHox structure further augments the adsorption capacity of the composite compared to pure GO and CNHox. The Ca²⁺ ions introduce basic sites with a high affinity for acidic gas molecules (e.g., CO₂), enabling chemical adsorption.⁴⁵

CONCLUSIONS

In summary, CNHox was successfully inserted into the interstitial spaces between GO lamellar nanosheets via the grafting of M ions, resulting in a novel GO–CNHox–M nanocomposite with higher porosity. This strategy effectively mitigated the aggregation tendency of the GO nanosheets, forming numerous nanowindows. Characterization data indicated that the pillaring of CNHox between GO nanosheets increased the layer spacing, with GO–CNHox–Ca exhibiting a higher CNHox content. N₂ adsorption results demonstrated that GO–CNHox–Ca had a higher SSA and a more advanced pore structure, with values of 374 m² g⁻¹ and 0.36 mL g⁻¹, respectively, which significantly exceeded those of GO. The newly formed composite material notably improved CO₂ capture due to its abundant nanowindows and mesoporous structure, resulting in increased CO₂ adsorption capacity.

ASSOCIATED CONTENT

Supporting Information

The Supporting Information is available free of charge at <https://pubs.acs.org/doi/10.1021/acs.langmuir.4c04479>.

SEM images, Wide-range XPS data, XRD pattern, TGA results, atomic composition and C/O ratios, and detailed data of specific surface areas and pore volumes (PDF)

AUTHOR INFORMATION

Corresponding Author

Takahiro Ohkubo – Department of Chemistry, Graduate School of Natural Science and Technology, Okayama University, Okayama 700-8530, Japan; orcid.org/0000-0001-5907-3683; Email: ohkubo@okayama-u.ac.jp

Authors

Zhao Li – Department of Chemistry, Graduate School of Natural Science and Technology, Okayama University, Okayama 700-8530, Japan

Moeto Toyota – Department of Chemistry, Graduate School of Natural Science and Technology, Okayama University, Okayama 700-8530, Japan

Complete contact information is available at:

<https://pubs.acs.org/10.1021/acs.langmuir.4c04479>

Author Contributions

Z.L.: Conceptualization, Methodology, Validation, Investigation, Data Curation, Visualization, Writing–Original Draft. M.T.: Investigation, Methodology. T.O.: Conceptualization, Methodology, Resources, Investigation, Visualization, Project administration, Supervision, Funding acquisition, Writing–review and editing.

Notes

The authors declare no competing financial interest.

ACKNOWLEDGMENTS

The authors appreciate Dr. Chiyu Nakano (Okayama University) for conducting the entrusted measurement of XPS.

REFERENCES

- (1) Yamada, Y.; Tanaka, H.; Kubo, S.; Sato, S. Unveiling Bonding States and Roles of Edges in Nitrogen-Doped Graphene Nanoribbon by X-Ray Photoelectron Spectroscopy. *Carbon* **2021**, *185*, 342–367.
- (2) Su, H.; Hu, Y. H. 3D Graphene: Synthesis, Properties, and Solar Cell Applications. *Chem. Commun.* **2023**, *59*, 6660–6673.
- (3) Sakamoto, R.; Toyoda, R.; Jingyan, G.; Nishina, Y.; Kamiya, K.; Nishihara, H.; Ogoshi, T. Coordination Chemistry for Innovative Carbon-Related Materials. *Coord. Chem. Rev.* **2022**, *466*, 214577–214581.
- (4) Du, W.; Wu, H.; Chen, H.; Xu, G.; Li, C. Graphene Oxide in Aqueous and Nonaqueous Media: Dispersion Behaviour and Solution Chemistry. *Carbon* **2020**, *158*, 568–579.
- (5) Majumder, P.; Gangopadhyay, R. Evolution of Graphene Oxide (GO)-Based Nanohybrid Materials with Diverse Compositions: An Overview. *RSC Adv.* **2022**, *12*, 5686–5719.
- (6) Marcano, D. C.; Kosynkin, D. V.; Berlin, J. M.; Sinitskii, A.; Sun, Z. Z.; Slesarev, A. S.; Alemany, L. B.; Lu, W.; Tour, J. M. Improved Synthesis of Graphene Oxide. *ACS Nano* **2010**, *4*, 4806–4814.
- (7) Dimiev, A. M.; Tour, J. M. Mechanism of Graphene Oxide Formation. *ACS Nano* **2014**, *8*, 3060–3068.
- (8) Park, J.; Lee, W.; Nam, J.; Han, J. T.; Choi, C. J.; Hwang, J. Y. A Study of the Correlation between the Oxidation Degree and Thickness of Graphene Oxides. *Carbon* **2022**, *189*, 579–585.

- (9) Costa, M. C. F.; Marangoni, V. S.; Ng, P. R.; Nguyen, H. T. L.; Carvalho, A.; Castro Neto, A. H. Accelerated Synthesis of Graphene Oxide from Graphene. *Nanomaterials* **2021**, *11*, 551–558.
- (10) Zhang, Y.; Mei, B.; Tian, X.; Jia, L.; Zhu, W. Remediation of Uranium(VI)-Containing Wastewater Based on a Novel Graphene Oxide/Hydroxyapatite Membrane. *J. Membr. Sci.* **2023**, *675*, 121543–121551.
- (11) Boulanger, N.; Li, G.; Bakhii, T.; Maslakov, K. I.; Romanchuk, A. Y.; Kalmykov, S. N.; Talyzin, A. V. Super-Oxidized “Activated Graphene” as 3D Analogue of Defect Graphene Oxide: Oxidation Degree vs U(VI) Sorption. *J. Hazard. Mater.* **2023**, *457*, 131817–131827.
- (12) Menezes, I. R. S.; Sakai, T.; Kaneko, K. Evaluation of Graphene Oxide Nanoporosity by Multiprobe Gas Adsorption Analysis. *J. Mater. Sci.* **2023**, *58*, 4439–4449.
- (13) Menezes, I. R. S.; Sakai, T.; Hattori, Y.; Kaneko, K. Effect of Preheating Temperature on Adsorption of N₂ and Ar on Graphene Oxide. *Chem. Phys. Lett.* **2022**, *807*, 140091–140097.
- (14) Sontakke, A. D.; Tiwari, S.; Purkait, M. K. A Comprehensive Review on Graphene Oxide-Based Nanocarriers: Synthesis, Functionalization and Biomedical Applications. *FlatChem* **2023**, *38*, 100484–100514.
- (15) Xiang, X.; Zhu, Y.; Gao, C.; Du, H.; Guo, C. Study on the Structure of Reduced Graphene Oxide Prepared by Different Reduction Methods. *Carbon Lett.* **2022**, *32*, 557–566.
- (16) Liyanage, C. D.; Kumar, H.; Perera, I.; Abeykoon, P. G.; Chen, F.; Joya, J. S.; Suib, S. L.; Adamson, D. H. Synthesis of Graphene Oxide: Effect of Sonication during Oxidation. *Carbon* **2024**, *223*, 119047–119053.
- (17) Zeng, W. J.; Li, C.; Feng, Y.; Zeng, S. H.; Fu, B. X.; Zhang, X. L. Carboxylated Multi-Walled Carbon Nanotubes (MWCNTs-COOH)-Intercalated Graphene Oxide Membranes for Highly Efficient Treatment of Organic Wastewater. *J. Water Proc. Eng.* **2021**, *40*, 101901–101908.
- (18) Sun, J.; Morales-Lara, F.; Klechikov, A.; Talyzin, A. V.; Baburin, I. A.; Seifert, G.; Cardano, F.; Baldrighi, M.; Frascioni, M.; Giordani, S. Porous Graphite Oxide Pillared with Tetrapod-Shaped Molecules. *Carbon* **2017**, *120*, 145–156.
- (19) Tran, M. L.; Tran, T. T. V.; Juang, R.-S.; Nguyen, C. H. Graphene Oxide Crosslinked Chitosan Composites for Enhanced Adsorption of Cationic Dye from Aqueous Solutions. *J. Taiwan Inst. Chem. Eng.* **2023**, *142*, 104678–104689.
- (20) Murata, K.; Kaneko, K.; Kanoh, H.; Kasuya, D.; Takahashi, K.; Kokai, F.; Yudasaka, M.; Iijima, S. Adsorption Mechanism of Supercritical Hydrogen in Internal and Interstitial Nanospaces of Single-Wall Carbon Nanohorn Assembly. *J. Phys. Chem. B* **2002**, *106*, 11132–11138.
- (21) Murata, K.; Kaneko, K.; Steele, W. A.; Kokai, F.; Takahashi, K.; Kasuya, D.; Hirahara, K.; Yudasaka, M.; Iijima, S. Molecular Potential Structures of Heat-Treated Single-Wall Carbon Nanohorn Assemblies. *J. Phys. Chem. B* **2001**, *105*, 10210–10216.
- (22) Kasuya, D.; Yudasaka, M.; Takahashi, K.; Kokai, F.; Iijima, S. Selective Production of Single-Wall Carbon Nanohorn Aggregates and Their Formation Mechanism. *J. Phys. Chem. B* **2002**, *106*, 4947–4951.
- (23) Bekyarova, E.; Hanzawa, Y.; Kaneko, K.; Silvestre-Albero, J.; Sepulveda-Escribano, A.; Rodriguez-Reinoso, F.; Kasuya, D.; Yudasaka, M.; Iijima, S. Cluster-Mediated Filling of Water Vapor in Intratube and Interstitial Nanospaces of Single-Wall Carbon Nanohorns. *Chem. Phys. Lett.* **2002**, *366*, 463–468.
- (24) Murata, K.; Kaneko, K.; Kokai, F.; Takahashi, K.; Yudasaka, M.; Iijima, S. Pore Structure of Single-Wall Carbon Nanohorn Aggregates. *Chem. Phys. Lett.* **2000**, *331*, 14–20.
- (25) Iijima, S.; Yudasaka, M.; Yamada, R.; Bandow, S.; Suenaga, K.; Kokai, F.; Takahashi, K. Nano-Aggregates of Single-Walled Graphitic Carbon Nano-Horns. *Chem. Phys. Lett.* **1999**, *309*, 165–170.
- (26) Garriga, R.; Jurewicz, I.; Seyedin, S.; Bardi, N.; Totti, S.; Matta-Domjan, B.; Velliou, E. G.; Alkhorayef, M. A.; Cebolla, V. L.; Razal, J. M.; et al. Multifunctional, Biocompatible and pH-Responsive Carbon Nanotube-and Graphene Oxide/Tectomer Hybrid Composites and Coatings. *Nanoscale* **2017**, *9*, 7791–7804.
- (27) Raza, A.; Altaf, S.; Ali, S.; Ikram, M.; Li, G. Recent Advances in Carbonaceous Sustainable Nanomaterials for Wastewater Treatments. *Sustain. Mater. Technol.* **2022**, *32*, e00406–e00455.
- (28) Park, S.; Lee, K.-S.; Bozoklu, G.; Cai, W.; Nguyen, S. T.; Ruoff, R. S. Graphene Oxide Papers Modified by Divalent Ions—Enhancing Mechanical Properties via Chemical Cross-Linking. *ACS Nano* **2008**, *2*, 572–578.
- (29) Xu, Y.; Zhao, L.; Bai, H.; Hong, W.; Li, C.; Shi, G. Chemically Converted Graphene Induced Molecular Flattening of 5,10,15,20-Tetrakis(1-methyl-4-pyridinio)porphyrin and Its Application for Optical Detection of Cadmium(II) Ions. *J. Am. Chem. Soc.* **2009**, *131* (37), 13490–13497.
- (30) Hummers, W. S., Jr.; Offeman, R. E. Preparation of Graphitic Oxide. *J. Am. Chem. Soc.* **1958**, *80*, 1339.
- (31) Kaneko, K.; Ishii, C. Superhigh Surface Area Determination of Microporous Solids. *Colloids Surf.* **1992**, *67*, 203–212.
- (32) Setoyama, N.; Suzuki, T.; Kaneko, K. Simulation Study on the Relationship between a High Resolution As-Plot and the Pore Size Distribution for Activated Carbon. *Carbon* **1998**, *36*, 1459–1467.
- (33) Thommes, M.; Kaneko, K.; Neimark, A. V.; Olivier, J. P.; Rodriguez-Reinoso, F.; Rouquerol, J.; Sing, K. S. W. Physisorption of Gases, with Special Reference to the Evaluation of Surface Area and Pore Size Distribution (IUPAC Technical Report). *Pure Appl. Chem.* **2015**, *87*, 1051–1069.
- (34) Stevic, D.; Furuse, A.; Vallejos-Burgos, F.; Kukobat, R.; Kaneko, K. Cu-Phthalocyanine-Mediated Nanowindow Production on Single-Wall Carbon Nanohorn. *Mol. Phys.* **2021**, *119*, No. e1815883.
- (35) Nagata, Y.; Kukobat, R.; Furuse, A.; Otsuka, H.; Hayashi, T.; Kaneko, K. Designed Production of Atomic-Scale Nanowindows in Single-Walled Carbon Nanotubes. *Langmuir* **2023**, *39* (16), 5911–5916.
- (36) Naghdi, S.; Song, H. Y.; Várez, A.; Rhee, K. Y.; Kim, S. W. Engineering the Electrical and Optical Properties of Graphene Oxide via Simultaneous Alkali Metal Doping and Thermal Annealing. *J. Mater. Res. Technol.* **2020**, *9*, 15824–15837.
- (37) Ma, J.; Liu, C.; Pu, F.; Wang, M.; Tian, S.; Li, H.; Zheng, H.; Wang, L.; Wang, C.; Yang, C.; et al. Constructing Pore Arrays on Nitrogen-Doped Carbon to Boost Potassium-Ion Storage Capacity. *Micropor. Mesopor. Mater.* **2022**, *341*, 112076–112086.
- (38) Wee, J.-H.; Kim, Y. A.; Yang, C.-M. Sequential Doping of Nitrogen and Oxygen in Single-Walled Carbon Nanohorns for Use as Supercapacitor Electrodes. *Micropor. Mesopor. Mater.* **2021**, *310*, 110595–110601.
- (39) Zhou, H.; Zhang, D. Effects of Interactions with Metal Ions on the Thermal Reduction of Graphene Oxide. *J. Phys. Chem. Solids* **2021**, *154*, 110090–110100.
- (40) Liu, Z.; Yang, Y.; Yuan, Y.; Wang, L.; Sheng, J.; Fei, W. Li⁺-Assisted Treatment of Graphene Oxide for Ultrahigh Volumetric Performance Supercapacitors. *J. Mater. Chem. A* **2022**, *10*, 10427–10438.
- (41) Zhao, G.; Zhu, H. Cation- π Interactions in Graphene-Containing Systems for Water Treatment and Beyond. *Adv. Mater.* **2020**, *32*, 1905756–1905777.
- (42) Singh, R.; Wang, L.; Ostrikov, K.; Huang, J. Designing Carbon-Based Porous Materials for Carbon Dioxide Capture. *Adv. Mater. Interfaces* **2024**, *11*, 2202290–2202317.
- (43) Al-Ghouti, M. A.; Da’ana, D. A. Guidelines for the Use and Interpretation of Adsorption Isotherm Models: A Review. *J. Hazard. Mater.* **2020**, *393*, 122383–122404.
- (44) Singh, G.; Lakhi, K. S.; Sil, S.; Bhosale, S. V.; Kim, I.; Albahily, K.; Vinu, A. Biomass Derived Porous Carbon for CO₂ Capture. *Carbon* **2019**, *148*, 164–186.
- (45) Xu, X.; Kan, Y.; Zhao, L.; Cao, X. Chemical Transformation of CO₂ during Its Capture by Waste Biomass Derived Biochars. *Environ. Pollut.* **2016**, *213*, 533–540.